

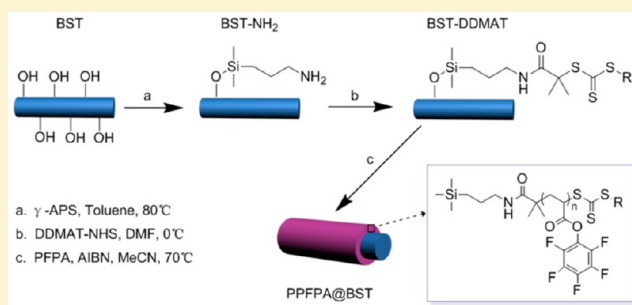
# Increasing the Energy Efficiency and Breakdown Strength of High-Energy-Density Polymer Nanocomposites by Engineering the Ba<sub>0.7</sub>Sr<sub>0.3</sub>TiO<sub>3</sub> Nanowire Surface via Reversible Addition–Fragmentation Chain Transfer Polymerization

Shen Wang,<sup>†</sup> Xingyi Huang,<sup>\*,†</sup> Guanyao Wang,<sup>†</sup> Yang Wang,<sup>†</sup> Jinliang He,<sup>‡</sup> and Pingkai Jiang<sup>†</sup>

<sup>†</sup>Shanghai Key Laboratory of Electrical Insulation and Thermal Aging, Department of Polymer Science and Engineering, Shanghai Jiao Tong University, Shanghai 200240, China

<sup>‡</sup>State Key Lab of Power Systems, Department of Electrical Engineering, Tsinghua University, Beijing 100084, China

**ABSTRACT:** Flexible nanocomposites comprising a dielectric polymer matrix and high-*k* nanoparticle fillers have shown great potential for power energy storage applications. However, the addition of high-*k* nanoparticles usually causes low breakdown strength and low energy efficiency of the nanocomposites, which limit their practical applications, particularly at high electric fields. In this work, we report a novel method to enhance the energy storage efficiency and breakdown strength of high-*k* nanowire (NW)-based poly(vinylidene fluoride-*co*-hexafluoropropylene) nanocomposites. Ba<sub>0.7</sub>Sr<sub>0.3</sub>TiO<sub>3</sub> NWs were synthesized by a hydrothermal method, and their surface was grafted with a layer of poly(pentafluorophenyl acrylate) (PPFPA) via in situ reversible addition–fragmentation chain transfer polymerization. Compared with the addition of as-prepared NWs, the incorporation of PPFPA-encapsulated NWs apparently enhanced the breakdown strength of the nanocomposites. On the other hand, the incorporation of PPFPA-encapsulated NWs results in much lower dielectric loss at low frequencies and higher energy storage efficiency of the nanocomposites. Although the two nanocomposites exhibit comparable discharged energy densities at relatively low electric field (e.g., <200 kV/mm), much higher energy storage capability can be expected in the nanocomposites with PPFPA-encapsulated NWs because of their high breakdown strength.



## INTRODUCTION

Dielectric materials with high dielectric constant and high breakdown strength have important applications in power energy storage devices (e.g., capacitors), weapon systems, and space technology.<sup>1–8</sup> The maximum energy density ( $U_{\max}$ ) of a dielectric material is normally described as

$$U_{\max} = \frac{1}{2} \epsilon \epsilon_0 E_b^2 \quad (1)$$

where  $E_b$  is the breakdown strength and  $\epsilon$  and  $\epsilon_0$  are the dielectric constants of the dielectric material and vacuum, respectively.<sup>1</sup> As is known to all, most high-dielectric-constant (high-*k*) materials are ceramics (e.g., BaTiO<sub>3</sub>). However, ceramics usually suffer from low dielectric strength and high processing difficulties.<sup>9,10</sup> Polymeric materials usually have the merits of high breakdown strength and ease of processing, but their intrinsic dielectric constants are much lower in comparison with ceramics.<sup>11</sup> In this case, composites comprising a polymer matrix and high-*k* ceramic filler have been extensively explored to serve as dielectric materials in high-energy-density devices.<sup>7,12–17</sup>

High-*k* ceramic nanoparticles rather than microsized particles have been widely used as fillers in preparing high-energy-

density polymer composites.<sup>10,18</sup> This is the case mainly because the thickness of the dielectric films used for high-energy-density devices is usually less than tens of micrometers, and ceramic fillers with small size tend to form uniform microstructures in the composite films. Compared with spherical high-*k* nanoparticles, high-aspect-ratio fillers such as nanowires (NWs) have been relatively seldom used to fabricate high-energy-density polymer nanocomposites because of their manufacturing challenges. However, it has been found in previous studies that high-aspect-ratio fillers can improve the dielectric constant of the nanocomposite more effectively compared with spherical particles.<sup>19–26</sup> Among the high-aspect-ratio high-*k* ceramic fillers, Ba<sub>x</sub>Sr<sub>1-x</sub>TiO<sub>3</sub> (BST) has attracted attention because of its low dielectric loss.<sup>27</sup> BST is a solid solution of BaTiO<sub>3</sub> and SrTiO<sub>3</sub>, and its dielectric constant reaches a maximum when the Ba mole fraction is about 0.71, while its dielectric loss tangent remains almost constant as the concentration of Ba varies.<sup>27,28</sup> To date, BST NWs have been used in the fabrication of high-energy-density polymer

**Received:** September 18, 2015

**Revised:** October 13, 2015

**Published:** October 15, 2015

nanocomposites.<sup>21,24,29</sup> Liu et al. prepared poly(vinylidene fluoride) (PVDF) nanocomposites consisting of surface-hydroxylated  $\text{Ba}_{0.6}\text{Sr}_{0.4}\text{TiO}_3$  (BST60) nanofibers.<sup>24</sup> The obtained nanocomposites exhibit their maximum energy density of  $6.4 \text{ J/cm}^3$  when the weight fraction of the BST60 nanofibers is 2.5%; this energy density is doubled that of pure PVDF.

It can be derived from eq 1 that the breakdown strength is the most important factor to determine the maximum energy density of dielectric materials. High breakdown strength is always desirable in order to maximize the energy storage capability. However, high- $k$  ceramics are inorganic fillers, which are usually incompatible with the organic matrix and tend to form agglomerates within the composites because of the large difference between the surface energies of the different components.<sup>30–32</sup> The formation of large-sized and irregular aggregates of the nanofiller results in low breakdown strength and high dielectric loss of the nanocomposites, which in turn lead to a decrease in the energy storage capability and energy efficiency, respectively. Therefore, it is important to improve the compatibility between the nanofiller and the polymer matrix. Ferroelectric polymers such as PVDF and its copolymers, such as poly(vinylidene fluoride-co-hexafluoropropylene) (P(VDF-HFP)), have been widely employed as polymer matrices because of their high intrinsic dielectric constants.<sup>19,33–36</sup> However, PVDF-based polymers have very low surface energies and thus are incompatible with most inorganic and organic materials.<sup>9</sup> Surface modification of the inorganic nanoparticles is usually needed to improve the nanoparticle/polymer compatibility when they are used as fillers. Two kinds of surface modifiers (i.e., organic small molecules and polymers) have been employed to functionalize the nanoparticles.<sup>20,37–46</sup> Organic small molecules such as coupling agents, which are easily grafted onto the nanoparticle surface, can reduce the surface energy of the nanoparticles and bridge the gap between the nanoparticles and the polymer matrix, resulting in improved nanoparticle/polymer compatibility.<sup>43,44,47,48</sup> However, the electrical property enhancement of the nanocomposites is usually limited because of the weak capability to tailor the physical properties of the interfacial phase of the nanocomposites. In contrast, grafting of polymers with well-defined thickness and electrical properties onto the nanoparticle surface is more powerful for the realization of large property enhancement of the nanocomposites.<sup>37–41</sup>

In this work, for the first time, poly(pentafluorophenyl acrylate)-encapsulated BST (PPFPA@BST) NWs were prepared via in situ reversible addition–fragmentation chain transfer (RAFT) polymerization, and the core–shell-structured PPFPA@BST NWs were used as fillers to fabricate P(VDF-HFP) nanocomposites for energy storage applications. The dielectric and energy storage properties of the corresponding PPFPA@BST and BST nanocomposites were explored in depth. It was demonstrated that both the energy efficiency and breakdown strength of the PPFPA@BST-based P(VDF-HFP) nanocomposites were increased in comparison with the BST nanocomposites.

## EXPERIMENTAL SECTION

**Materials.** Titanium dioxide nanopowder ( $\text{TiO}_2$ , P25,  $\geq 99.5\%$ ) was purchased from Sigma-Aldrich. Barium hydroxide octahydrate ( $\text{Ba}(\text{OH})_2 \cdot 8\text{H}_2\text{O}$ , ACS, 98%) and strontium hydroxide octahydrate ( $\text{Sr}(\text{OH})_2 \cdot 8\text{H}_2\text{O}$ , ACS, 99.5%) were supplied by Aladdin (Shanghai, China). *N*-Hydroxysuccinimide (NHS), *N,N'*-dicyclohexylcarbodiimide (DCC), 4-dimethyla-

minopyridine (DMAP), ( $\gamma$ -aminopropyl)triethoxysilane ( $\gamma$ -APS), and the RAFT agent *S*-1-dodecyl-*S'*-( $\alpha,\alpha'$ -dimethyl- $\alpha''$ -acetic acid) trithiocarbonate (DDMAT) were all purchased from Acros. Pentafluorophenyl acrylate (PFPA) was provided by Suzhou Highfine Biotechnology Co., Ltd. (Suzhou, China). P(VDF-HFP) with 15% HFP was supplied by Solvay Plastics (Shanghai, China). Other chemicals or reagents were purchased from Sinopharm Chemical Reagent Co., Ltd. (Shanghai, China). Among these reagents, PFPA monomer was passed through a basic alumina column before use, and the others were used as received except for special notes.

**Synthesis of  $\text{Ba}_{0.7}\text{Sr}_{0.3}\text{TiO}_3$  NWs.**  $\text{Ba}_{0.7}\text{Sr}_{0.3}\text{TiO}_3$  (BST) NWs were fabricated by a two-step hydrothermal reaction. The first step was to synthesize sodium titanate ( $\text{Na}_2\text{Ti}_3\text{O}_7$ ) NWs as an intermediate product according to previous literature.<sup>49,50</sup> First, 3 g of  $\text{TiO}_2$  nanopowder was mixed with 60 mL of 10 M aqueous NaOH solution. The mixed solution was then stirred for 24 h, sealed in a 90 mL Teflon autoclave, and maintained in an oven at  $200^\circ\text{C}$  for 3 days. The resultant  $\text{Na}_2\text{Ti}_3\text{O}_7$  NWs were washed with deionized water and ethanol until pH-neutral and then soaked in a 0.1 M hydrochloric acid aqueous solution for 12 h to produce hydrogen titanate ( $\text{H}_2\text{Ti}_3\text{O}_7$ ) NWs. The obtained  $\text{H}_2\text{Ti}_3\text{O}_7$  NWs were subsequently dried in a vacuum oven at  $100^\circ\text{C}$ .

A second hydrothermal reaction was then employed to synthesize  $\text{Ba}_{0.7}\text{Sr}_{0.3}\text{TiO}_3$  NWs according to Tang's method.<sup>21–23,27</sup>  $\text{Ba}(\text{OH})_2 \cdot 8\text{H}_2\text{O}$  (0.804 g,  $2.55 \times 10^{-3}$  mol) and  $\text{Sr}(\text{OH})_2 \cdot 8\text{H}_2\text{O}$  (0.120 g,  $0.45 \times 10^{-3}$  mol) were added to  $\text{H}_2\text{Ti}_3\text{O}_7$  (0.129 g,  $5 \times 10^{-4}$  mol) to fully transform the  $\text{H}_2\text{Ti}_3\text{O}_7$  NWs to  $\text{Ba}_{0.7}\text{Sr}_{0.3}\text{TiO}_3$  NWs in a 90 mL Teflon autoclave. The mixture was stirred for 24 h and then heated at  $210^\circ\text{C}$  for 85 min. The obtained NWs were rinsed several times with 0.1 M aqueous hydrochloric acid solution, deionized water, and ethanol.

**Activation of the RAFT Agent DDMAT.** The activation of DDMAT was conducted according to the reported method.<sup>51,52</sup> The typical procedure was as follows: DDMAT (0.36 g, 1.0 mmol), NHS (0.14 g, 1.2 mmol), and DMAP (0.012 g, 0.1 mmol) were dissolved in dry  $\text{CH}_2\text{Cl}_2$  (20 mL). Then DCC (0.25 g, 1.2 mmol) in  $\text{CH}_2\text{Cl}_2$  (10 mL) was added to the mixture slowly at  $-10^\circ\text{C}$ . The mixture was stirred for 12 h at room temperature and then filtered to remove the precipitate. Activated DDMAT (NHS-DDMAT) was finally obtained as yellow crystals (0.39 g, 85% yield) after removal of the solvent and chromatographic separation (silica gel, eluting with 5:3 (v/v) petroleum ether/ethyl acetate).

**Preparation of Amino-Functionalized  $\text{Ba}_{0.7}\text{Sr}_{0.3}\text{TiO}_3$  NWs.** The amino-functionalized BST NWs were prepared according to previous literature.<sup>52,53</sup>  $\text{Ba}_{0.7}\text{Sr}_{0.3}\text{TiO}_3$  NWs (5 g) and toluene (100 mL) were combined in a 250 mL three-neck round-bottom flask and sonicated for 30 min, after which  $\gamma$ -APS (3 g) was added. The resulting mixture was refluxed at  $80^\circ\text{C}$  for 24 h under a  $\text{N}_2$  atmosphere with vigorous stirring. The NWs were recovered by centrifugation at 9000 rpm for 5 min and washed with toluene three times. The obtained amino-functionalized  $\text{Ba}_{0.7}\text{Sr}_{0.3}\text{TiO}_3$  (BST-NH<sub>2</sub>) NWs were dried under vacuum at  $80^\circ\text{C}$  for 24 h.

**Preparation of DDMAT-Anchored  $\text{Ba}_{0.7}\text{Sr}_{0.3}\text{TiO}_3$  NWs.** The obtained BST-NH<sub>2</sub> NWs were further reacted with NHS-DDMAT to yield RAFT-agent-functionalized BST (BST-DDMAT) NWs.<sup>52</sup> BST-NH<sub>2</sub> NWs (5 g) were dispersed in *N,N*-dimethylformamide (DMF) and sonicated for 30 min. Then the mixture was added dropwise to a toluene



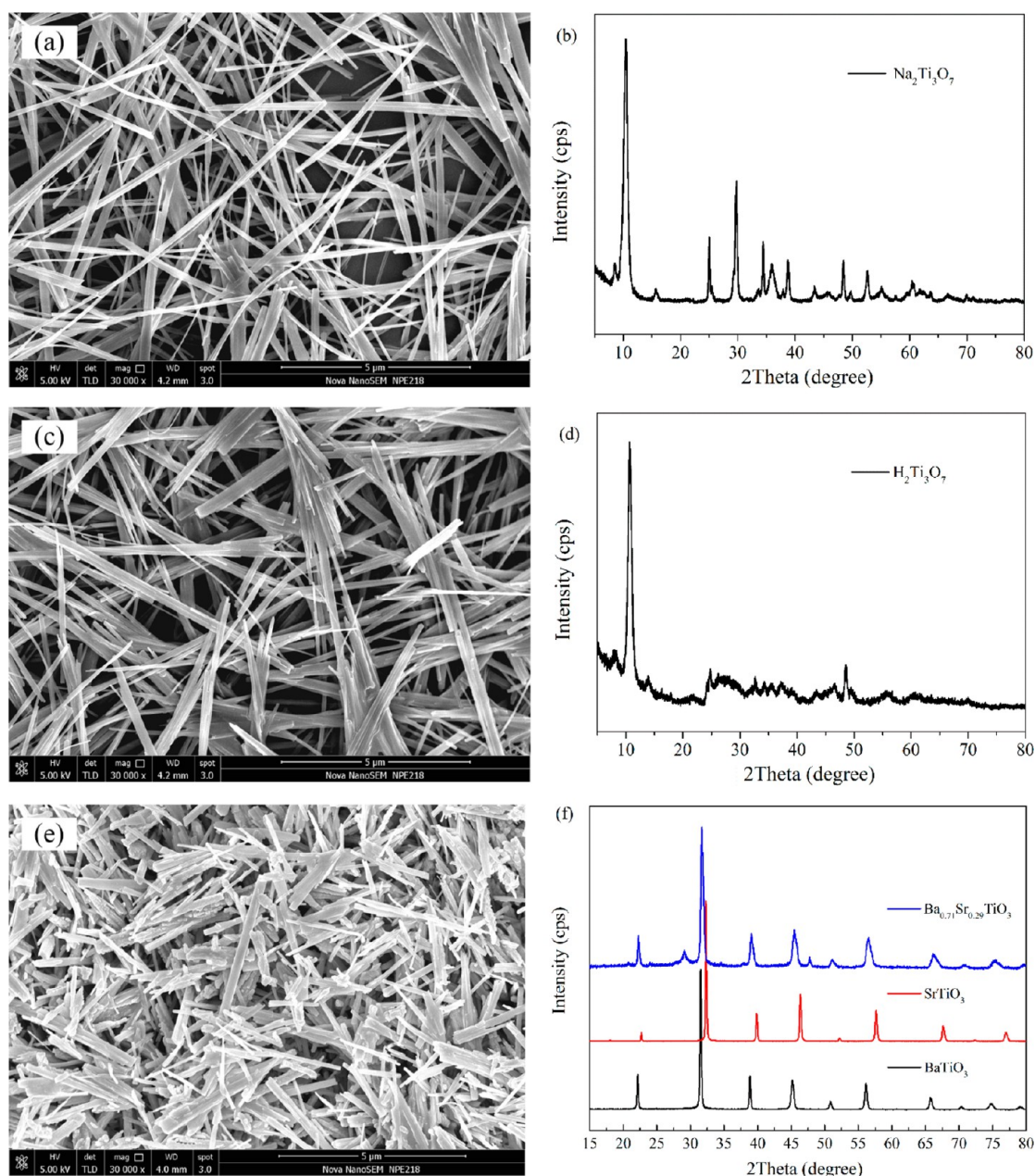


**Figure 1.** (a, c, e) SEM images and (b, d, f) XRD patterns of (a, b)  $\text{Na}_2\text{Ti}_3\text{O}_7$ , (c, d)  $\text{H}_2\text{Ti}_3\text{O}_7$ , and (e, f) BST NWs

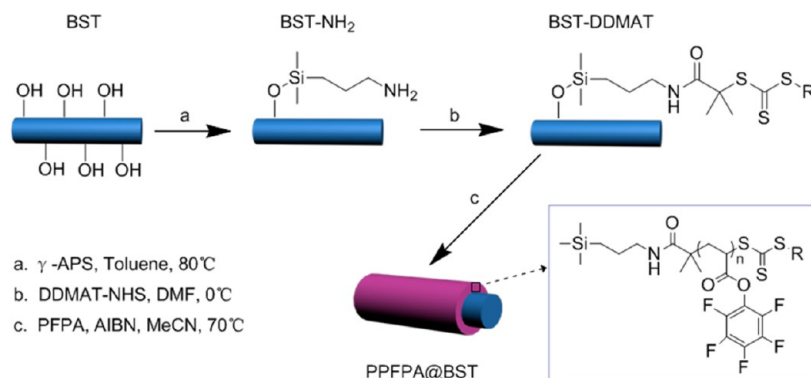
solution of NHS–DDMAT at 0 °C with vigorous stirring. The reaction mixture was kept at 0 °C for 6 h, allowed to gradually warm to room temperature, and then left to stir for 12 h. The mixture was precipitated into a large amount of toluene after the reaction, and centrifugation afforded BST–DDMAT. The pristine BST–DDMAT was washed with DMF and ethanol and then dried under vacuum at 60 °C for 24 h.

**Surface-Initiated RAFT Polymerization of PFPa from  $\text{Ba}_{0.7}\text{Sr}_{0.3}\text{TiO}_3$  NWs.** The typical procedure was carried out as follows: To a 25 mL round-bottom flask were added BST–DDMAT (0.5 g, 0.0241 mmol), free RAFT agent DDMAT (1.2 mg, 0.0033 mmol), acetonitrile (MeCN, 3 mL), and PFPa (3 g, 12.6 mmol). After sonication, azobis(isobutyronitrile) (AIBN) (1.6 mg, 0.0097 mmol) was added. Then the flask was sealed with a rubber plug, and the solution was deoxygenated by purging with nitrogen gas for 40 min. The flask was placed in an oil bath at 70 °C for 12 h with magnetic stirring. The

polymerization was halted by cooling and exposure to air. The solution was diluted with MeCN and centrifuged to decant the supernatant. Then the pristine PFPa@BST was washed with DMF four times. The product was dried under vacuum at 80 °C for 24 h.

**Fabrication of P(VDF–HFP)-Based Nanocomposite Films.** The typical process for fabricating P(VDF–HFP)-based nanocomposite films was as follows: PFPa@BST was dispersed in DMF, and the dispersion was heated at 80 °C for 30 min and then sonicated for 20 min. Meanwhile, P(VDF–HFP) was dissolved in DMF, and the solution was stirred for 30 min. The dispersion and solution were then mixed and stirred vigorously for 24 h. The mixture was ultrasonicated with a piezoelectric vibrator for another 3 min before casting on a glass plate. The films were dried at 100 °C for 2 h and then kept under vacuum at the same temperature for 12 h to remove the solvent thoroughly. The obtained films were subsequently

Scheme 1. Schematic Illustration of the Synthesis of PPFPA@BST NWs by Surface-Initiated RAFT Polymerization



molded by hot-pressing at 200 °C. The thickness of the films was around 30  $\mu\text{m}$ . The volume percentages of BST NWs in the PPFPA@BST/P(VDF–HFP) nanocomposites were 2.5%, 5%, 7.5%, and 10%. BST/P(VDF–HFP) and P(VDF–HFP) films were prepared in the same way, and the volume percentages of BST NWs in the BST/P(VDF–HFP) films were also 2.5%, 5%, 7.5%, and 10%, respectively.

**Characterization.** The crystalline structure of the NWs were analyzed by X-ray diffraction (XRD) using an X-ray diffractometer (D/max-2200/PC, Rigaku, Tokyo, Japan) with a Cu  $K\alpha$  source. Scanning electron microscopy (SEM) (Nova NanoSEM 450, FEI, Hillsboro, OR, USA) and transmission electron microscopy (TEM) (JEM-2010, JEOL, Tokyo, Japan) were applied to characterize the morphologies of the NWs and the nanocomposite samples. The functionalized NW samples were prepared by dropping a few drops of the sample solution on silicon chips (for SEM) or microgrids (for TEM) and drying in the air before measurement. The cross-sectional SEM images of nanocomposite films were obtained on samples prepared by fracturing the films in liquid nitrogen, and the TEM cross-sectional samples were obtained by ultramicrotomy.  $^1\text{H}$  NMR spectra of different samples were recorded with a Varian Mercury Plus 400 MHz spectrometer in  $\text{CDCl}_3$  using tetramethylsilane as the standard. Fourier transform infrared (FT-IR) spectroscopy with a PerkinElmer Paragon 1000 spectrometer was used to characterize the chemical structures of the pristine and surface-modified NWs over the range of 4000–400  $\text{cm}^{-1}$ . X-ray photoelectron spectroscopy (XPS) of the NWs was conducted using an Axis Ultra spectrometer (Kratos Analytical, Manchester, UK) with a monochromatized Al  $K\alpha$  source. A NETZSCH TG209 F3 thermo-microbalance was used to perform the thermogravimetric analysis (TGA) of NWs at a heating rate of 20 °C/min in a nitrogen flow (20 mL/min). The dielectric properties of the samples were measured using a Concept 40 dielectric spectrometer equipped with an Alpha-N high-resolution dielectric analyzer (Novocontrol Technologies GmbH, Hundsangen, Germany) over the frequency range  $10^{-1}$ – $10^6$  Hz at room temperature. Layers of gold were evaporated on both sides of the samples to serve as electrodes. The direct-current breakdown strength was measured using a dielectric strength tester with a ball-to-ball stainless electrode (DH, Shanghai Lanpotronics Co., Shanghai, China). The samples used for these measurements all had a thickness of around 50  $\mu\text{m}$ . Electric displacement–electric field ( $D$ – $E$ ) loops and two-probe current–voltage ( $I$ – $V$ ) measurements were conducted using a Precision multiferroic materials analyzer equipped with a Precision 10 kV single-channel high-

voltage interface (Radiant Technologies, Albuquerque, NM, USA) and a high-voltage power amplifier (model 609B, Trek, Lockport, NY, USA). Both sides of the samples were sputtered with gold to form 3 mm diameter electrodes.

## RESULTS AND DISCUSSION

**Preparation and Characterization of PPFPA@BST NWs.** The BST NWs were synthesized by a two-step hydrothermal reaction. Figure 1 shows SEM images and XRD patterns of the products of different steps. The XRD patterns confirm the structure of these products, which were  $\text{Na}_2\text{Ti}_3\text{O}_7$ ,  $\text{H}_2\text{Ti}_3\text{O}_7$ , and BST NWs, respectively.  $\text{Na}_2\text{Ti}_3\text{O}_7$  NWs were obtained from the first hydrothermal reaction. However,  $\text{H}_2\text{Ti}_3\text{O}_7$  NWs instead of  $\text{Na}_2\text{Ti}_3\text{O}_7$  NWs were chosen to be the precursor of the BST NWs because of their open structure, which is more suitable for ion exchange.<sup>54,55</sup> The synthesis of BST NWs was subsequently carried out by another hydrothermal reaction. According to previous literature, BST is a solid solution of  $\text{BaTiO}_3$  and  $\text{SrTiO}_3$ , and the mole fraction of barium in the solid solution can affect the Curie temperature, which in turn affects the dielectric constant of the NWs.<sup>27,28</sup> It has been found that when the composition of the NWs is  $\text{Ba}_{0.71}\text{Sr}_{0.29}\text{Ti}_3\text{O}_7$ , the NWs have the highest dielectric constant and the crystals of the NWs remain a ferroelectric phase. The mole fraction of barium in the solid solution can be adjusted by varying the initial concentrations of barium and strontium in the reactant solution. When the feed ratio is  $\text{Ba}/(\text{Ba} + \text{Sr}) = 0.85$ , the Ba/Sr stoichiometry in the BST NWs is around 0.71/0.29.<sup>27</sup> The XRD patterns shown in Figure 1 demonstrate the successful introduction of barium and strontium ions, as designed.

Scheme 1 illustrates the preparation process of the core–shell-structured PPFPA@BST NWs. PPFPA was designed to be grafted onto the NW surface via in situ RAFT polymerization.<sup>39</sup> To achieve such a target, the RAFT agent (i.e., DDMAT) had to be grafted onto the NWs. However, aminolysis of the thioester groups of DDMAT agent would occur via reaction with amino groups from the silanes grafted onto the nanoparticle surface. Therefore, DDMAT was first activated by NHS to keep the thioester groups of the RAFT agent from aminolysis. Figure 2 shows the  $^1\text{H}$  NMR spectra of DDMAT and NHS–DDMAT. The proton signals appear in the NHS–DDMAT spectrum at 2.81 ppm (peak e), indicating that DDMAT was successfully activated. Surface grafting of the silane coupling agent on the surface of the BST NWs was confirmed by FT-IR spectra. One can see from Figure 3a that compared with the FT-IR spectrum of as-prepared BST, the

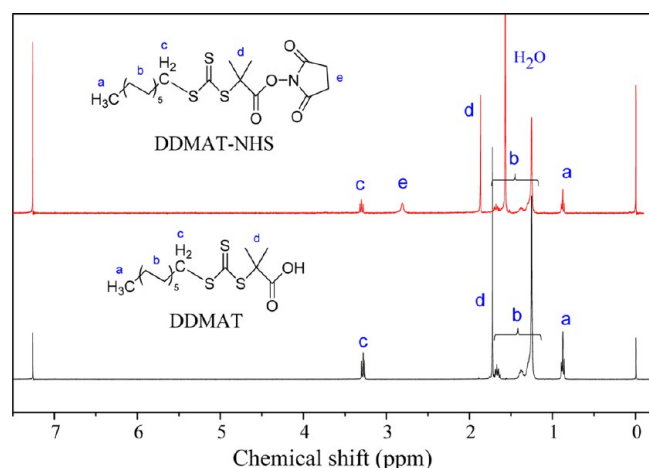


**Figure 2.**  $^1\text{H}$  NMR spectra of DDMAT and DDMAT-NHS in  $\text{CDCl}_3$ .

spectrum of BST-NH<sub>2</sub> shows new absorption bands at 1148 and 1382  $\text{cm}^{-1}$ , which are attributed to the stretching vibration of the Si-O-BST bond and bending vibration of the C-H bonds, respectively. For BST-DDMAT, a new absorption band appears at 1642  $\text{cm}^{-1}$  (amide C=O stretching vibration), suggesting that DDMAT was anchored onto the BST NWs. In addition, the appearance of the proton signals of CH<sub>3</sub> and CH<sub>2</sub> of BST-DDMAT in the  $^1\text{H}$  NMR spectrum (Figure 3b) also confirms the successful grafting of DDMAT onto the BST NWs. The last step was the preparation of PPFPA@BST via in situ RAFT polymerization. As shown in Figure 3a, a new absorption peak appeared at 1776  $\text{cm}^{-1}$  in the FT-IR spectrum

of PPFPA@BST, which is attributed to the ester C=O stretching vibration. This observation, in combination with the proton signals appearing at around 2 and 3 ppm at the  $^1\text{H}$  NMR spectrum of PPFPA@BST (Figure 3b), indicates that PPFPA was successfully introduced onto the surface of the BST NWs.

XPS (Figure 3c) and TGA (Figure 3d) were also used to prove the successful completion of the surface modification of BST NWs. The successive appearance of the binding peaks of N, S, and F in the XPS spectra and the increasing weight loss from BST to PPFPA@BST are both consistent with the conclusion inferred from the FT-IR and  $^1\text{H}$  NMR spectra.

Figure 4 shows SEM and TEM images of a PPFPA@BST nanowire. One can see that the BST NWs have been completely encapsulated by a layer of PPFPA. Furthermore, the TEM image shows that the thickness of PPFPA shell is about 5 nm.

#### Microstructure of the P(VDF-HFP) Nanocomposites.

PPFPA@BST/P(VDF-HFP) nanocomposites with BST volume percentages of 2.5%, 5%, 7.5%, and 10% were prepared by solution blending followed by hot-pressing. For comparison, BST/P(VDF-HFP) nanocomposites with the same volume fractions of as-prepared BST NWs (without any modification on the surface) were also fabricated as control samples. Figure 5 shows SEM images of freeze-fractured cross sections of nanocomposites with 10% BST. It seems that the PPFPA@BST/P(VDF-HFP) nanocomposites exhibit better compatibility between the NWs and the polymer matrix in comparison with the BST/P(VDF-HFP) nanocomposites. The PPFPA@BST displays improved adhesion to the polymer matrix, and there is no evident debonding between the NWs and the

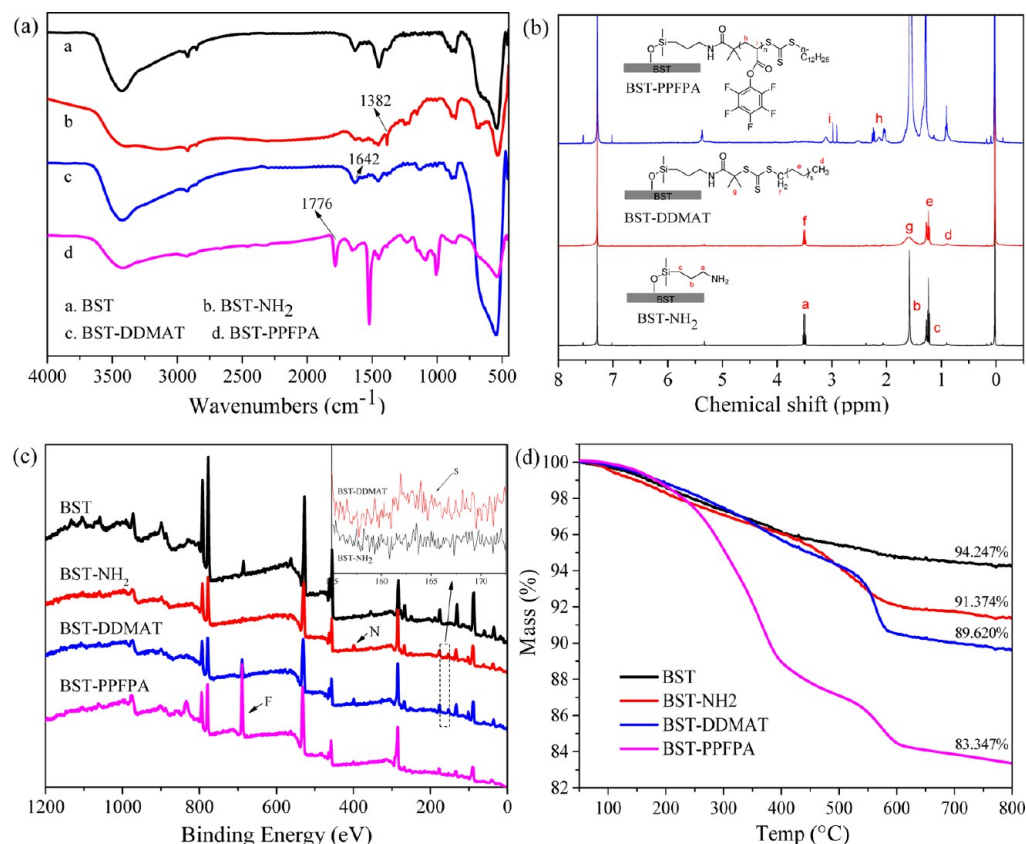


**Figure 3.** (a) FT-IR spectra, (b)  $^1\text{H}$  NMR spectra in  $\text{CDCl}_3$ , (c) XPS spectra, and (d) TGA curves of functionalized BST NWs.



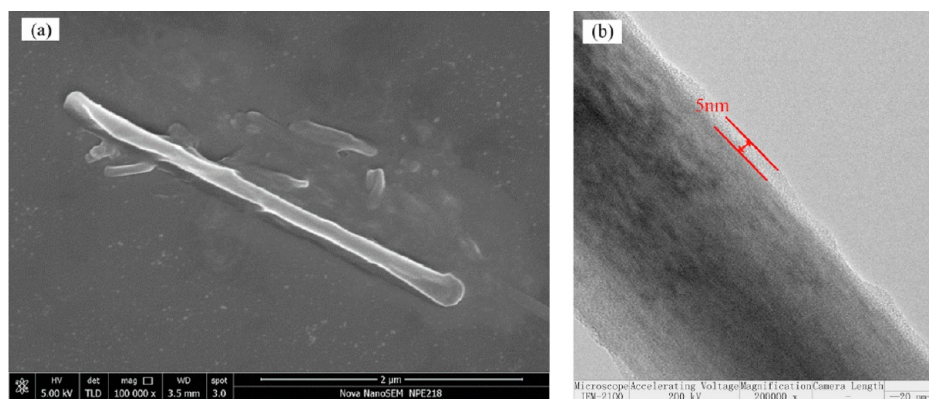


**Figure 4.** (a) SEM and (b) TEM images of PPFPA@BST nanowires.

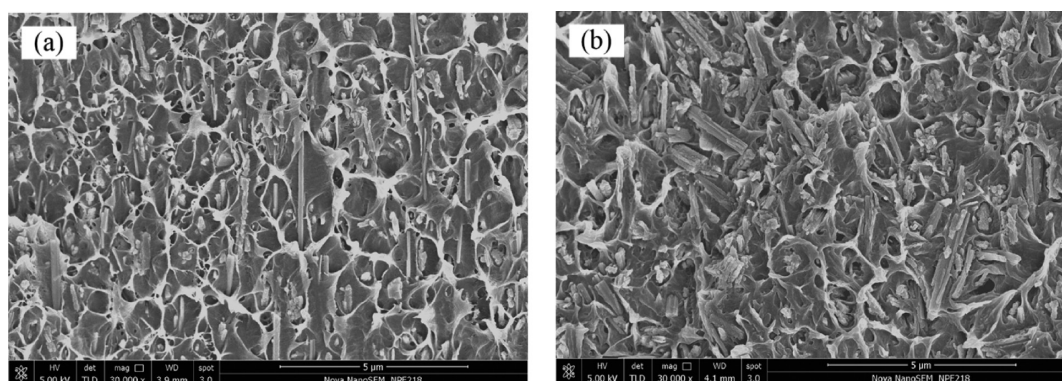


**Figure 5.** SEM images of freeze-fractured cross sections of (a) BST/P(VDF-HFP) and (b) PPFPA@BST/P(VDF-HFP) nanocomposites with 10 vol % BST.

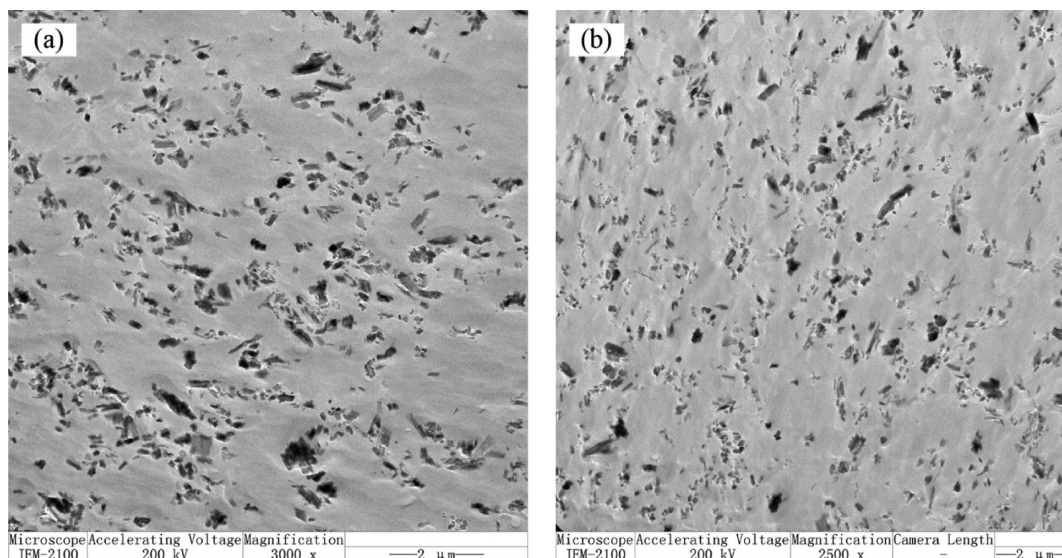


**Figure 6.** TEM images of (a) BST/P(VDF-HFP) and (b) PPFPA@BST/P(VDF-HFP) nanocomposites with 10 vol % BST.

polymer matrix. The as-prepared BST NWs, however, show relatively weak adhesion to the polymer matrix. The excellent compatibility between PPFPA@BST NWs and P(VDF-HFP) can be ascribed to two factors: (i) the strong dipole–dipole interactions between the carbonyl groups in the PPFPA chains and the fluorine atoms in the P(VDF-HFP) chains and (ii) the similar chemical structures and surface energies of the PPFPA shell and the P(VDF-HFP) matrix.

TEM was used to further observe the dispersion of BST NWs in the P(VDF-HFP) matrix. **Figure 6** presents TEM images of the BST/P(VDF-HFP) and PPFPA@BST/P(VDF-HFP) nanocomposites. It seems that the BST NWs are homogeneously and randomly scattered in the PPFPA@BST/P(VDF-HFP) nanocomposites, while agglomerations can be found in the BST/P(VDF-HFP) nanocomposites. All of these results explicitly declare that the grafting of the PPFPA

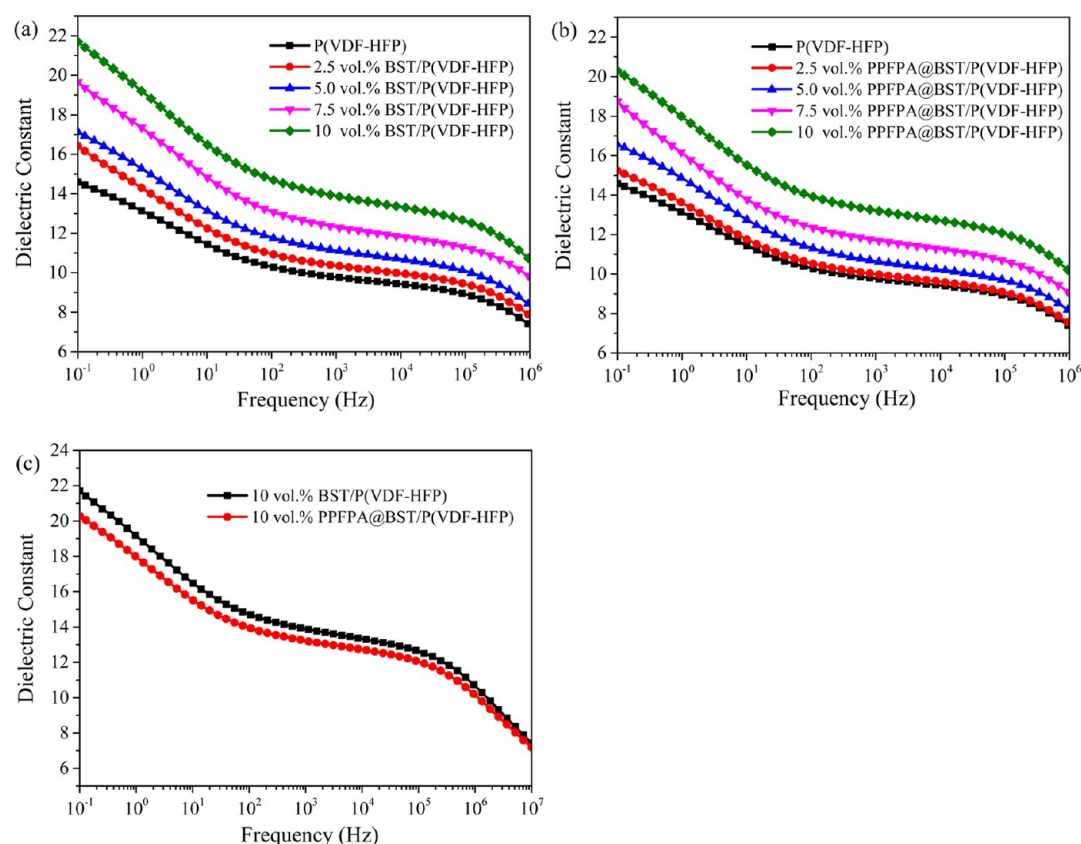


**Figure 7.** (a, b) Frequency-dependent dielectric constants of the (a) BST/P(VDF–HFP) and (b) PPFPA@BST/P(VDF–HFP) nanocomposites. (c) Comparison of the dielectric constants of BST/P(VDF–HFP) and PPFPA@BST/P(VDF–HFP) with 10 vol % BST. (d) Comparison of the dielectric constants of PPFPA and P(VDF–HFP).

shell can facilitate the dispersion of BST NWs in the P(VDF–HFP) matrix.

**Dielectric Properties of the P(VDF–HFP) Nanocomposites.** The dielectric properties of the P(VDF–HFP) nanocomposite films were measured using a broadband dielectric spectrometer from 0.1 Hz to 1 MHz at room temperature. Figure 7 shows that the dielectric constant of the nanocomposite films increases gradually as the loading of BST NWs increases. This occurs mainly because the dielectric constant of the BST NWs is much larger than that of the polymer matrix. Compared with the BST/P(VDF–HFP) nanocomposites, the PPFPA@BST/P(VDF–HFP) nanocomposites have a slightly lower dielectric constant at the same NW loading. A decrease in the dielectric constant in polymer nanocomposites with surface-functionalized nanoparticles has frequently been observed.<sup>41,56</sup> The possible reasons may be associated with the filler dispersion state, variation of the electrical properties (e.g., dielectric constant, conductivity) of the filler surface, and the interfacial polarization.

The filler dispersion state may not play an important role in increasing the dielectric constant of the BST/P(VDF–HFP) nanocomposites. According to the numerical simulation results of Dang et al.,<sup>57</sup> the dispersion state has only a marginal influence (about  $\pm 3\%$ ) on the dielectric constant of particulate composites.

Here the lower dielectric constant of PPFPA@BST/P(VDF–HFP) should be first attributed to the lower dielectric constant of the interfacial region in the nanocomposites. The interfacial region of PPFPA@BST/P(VDF–HFP) is mainly composed of the PPFPA shell covalently linked with the NWs,

while in BST/P(VDF–HFP) the interfacial region is composed of surface functional groups of the NWs (e.g., –OH) and P(VDF–HFP). The surface functional groups usually have large dipole moments, resulting in a high dielectric constant of the NW surface. On the other hand, the lower dielectric constant of PPFPA was demonstrated by broadband dielectric spectroscopy measurement. As shown in Figure 7d, PPFPA exhibits much a lower dielectric constant in comparison with P(VDF–HFP) over the whole measured frequency range.

Second, the effect of the weak interfacial polarization in PPFPA@BST/P(VDF–HFP) should not be neglected. The as-prepared BST NWs exhibit weak adhesion to the P(VDF–HFP) matrix. On the other hand, the as-prepared BST NWs may have higher surface conductivity because of the existence of unreacted functional groups. These two factors may facilitate the movement and accumulation of charge carriers, resulting in strong interfacial polarization. The grafting of PPFPA onto the surface of the BST NWs not only enhances the interfacial interaction between PPFPA@BST and P(VDF–HFP) but also reduces the amounts of free functional groups, resulting in weak interfacial polarization in the PPFPA@BST/P(VDF–HFP) nanocomposites.

Figure 8 shows the frequency-dependent dielectric loss tangents of the PPFPA@BST/P(VDF–HFP) and BST/P(VDF–HFP) nanocomposites. One can see that compared with the P(VDF–HFP) matrix, the two types of nanocomposites display similar dielectric loss tangents at high frequencies and enhanced dielectric loss tangents at low frequencies. However, it should be noted that compared with the PPFPA@BST/P(VDF–HFP) nanocomposites, the en-

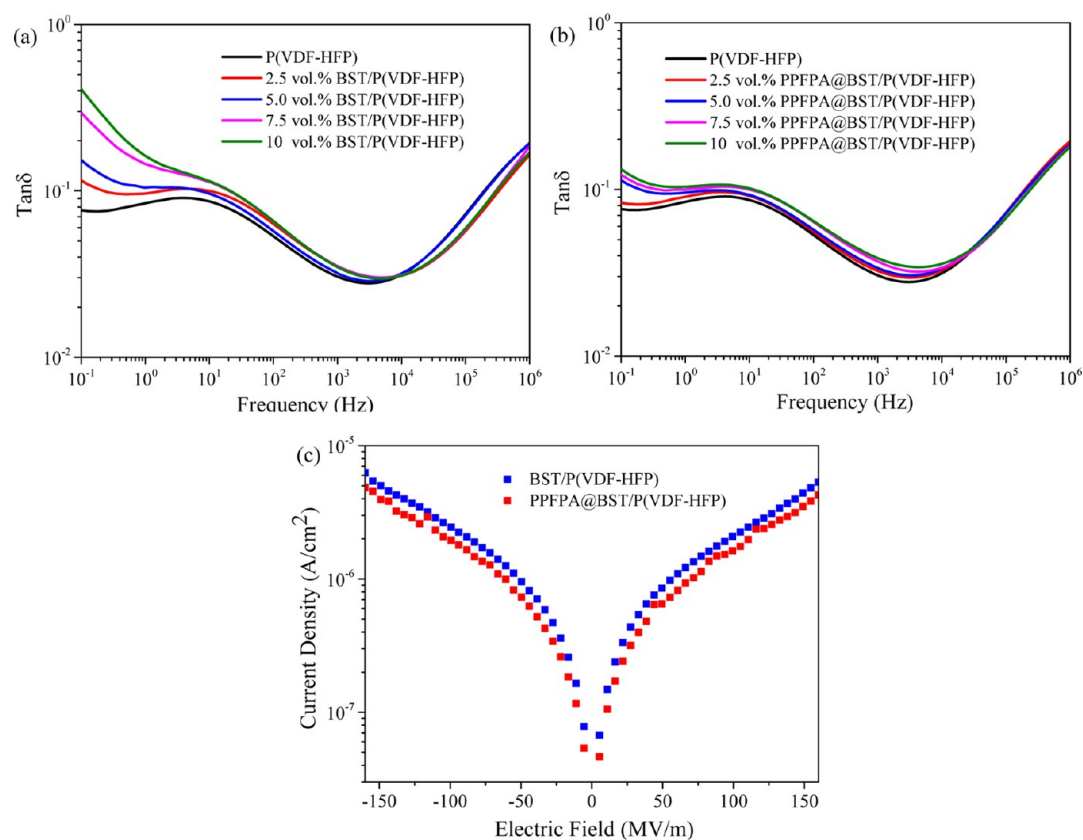


**Figure 8.** (a, b) Frequency dependence of the dielectric loss tangents of the (a) BST/P(VDF-HFP) and (b) PPFPA@BST/P(VDF-HFP) nanocomposites. (c) Leakage current densities of the BST/P(VDF-HFP) and PPFPA@BST/P(VDF-HFP) nanocomposites with 10% BST NWs.

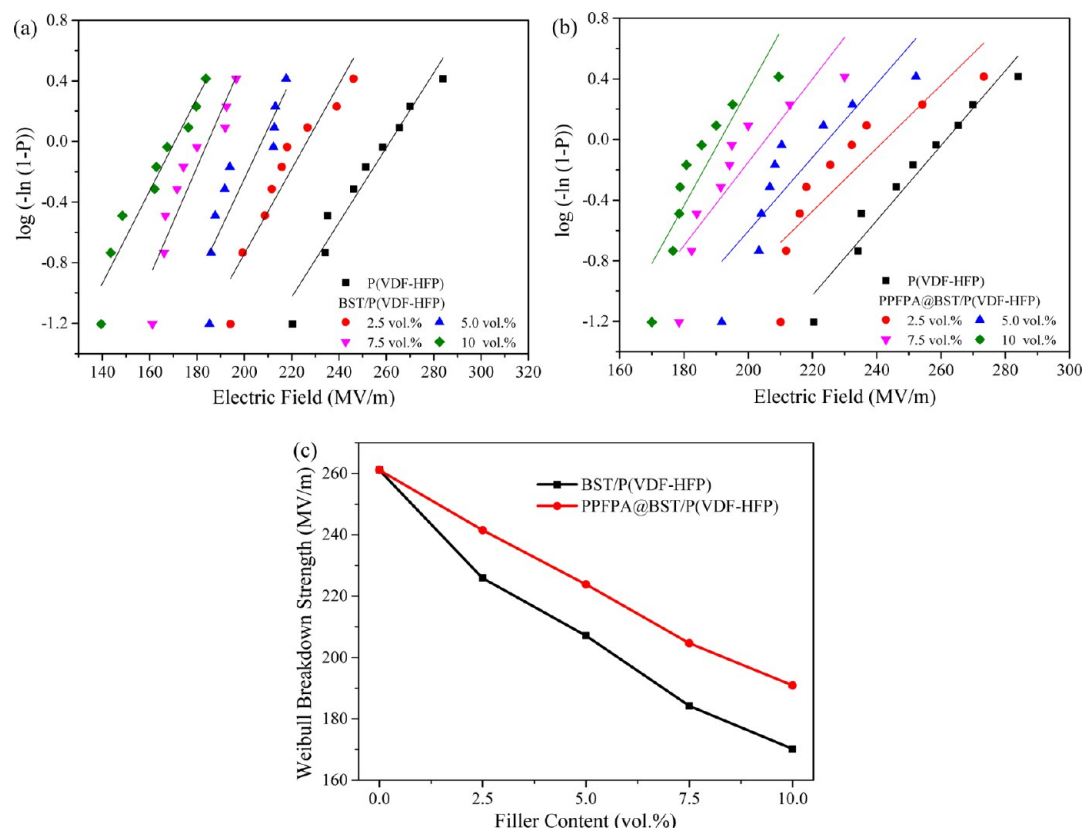


**Figure 9.** (a, b) Weibull plots of breakdown strength and (c) comparison of the characteristic breakdown strengths of the P(VDF-HFP) nanocomposites.



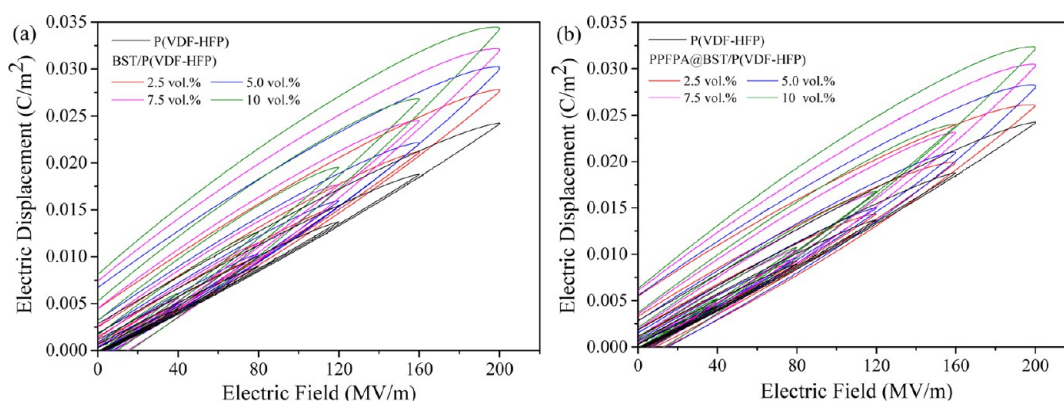


**Figure 10.** Electric displacement–electric field ( $D$ – $E$ ) loops of BST/P(VDF–HFP) and PPFPA@BST/P(VDF–HFP) nanocomposites versus electric field at room temperature.

hancement of the dielectric loss tangent in the BST/P(VDF–HFP) nanocomposites is much higher at superlow frequencies. The enhancement of the dielectric loss tangent in the nanocomposites should be ascribed to the increase in the number of mobile charge carriers.<sup>40,58</sup> The incorporation of NWs not only introduces additional charge carriers but also provides paths for charge carrier transport. The small increase in the dielectric loss tangent in the PPFPA@BST/P(VDF–HFP) nanocomposites should be attributed to the good interfacial adhesion between fluoro-modified NWs and the P(VDF–HFP) and the covalent linking between PPFPA and BST. The former limits the movement of charge carriers, whereas the latter reduces the number of charge carriers. The decrease in the leakage current in the PPFPA@BST/P(VDF–HFP) nanocomposites evidences the decreased number and/or mobility of the charge carriers. Taking the nanocomposites with 10 vol % NWs as an example, as shown in Figure 8c, the PPFPA@BST/P(VDF–HFP) nanocomposite sample exhibits decreased leakage currents no matter how high the electric field is (here, from 0 to 160 kV/mm). In addition, although the nanocomposites exhibit enhanced leakage currents in comparison with the P(VDF–HFP) matrix, the electrical resistivities of the PPFPA@BST/P(VDF–HFP) nanocomposites are all in the range of  $10^{11}$ – $10^{12}$   $\Omega$ ·cm, which is still at the same level as that of pure P(VDF–HFP), demonstrating the favorable insulating properties of the obtained nanocomposites for practical applications.

**Breakdown Strength of the P(VDF–HFP) Nanocomposites.** High breakdown strength is highly desirable to achieve an energy storage capability that is as large as possible. It is known that the breakdown strength of the nanocomposites is closely associated with the electrical properties (e.g., electrical conductivity and dielectric constant) and the concentration of filler. Significantly reduced breakdown strength is usually observed when the filler loading is high and the dielectric constant and electrical conductivity are much higher than those of the polymer matrix. To maintain high breakdown strength of the nanocomposites, the volume fraction of BST NWs was designed to be no more than 10%. The Weibull plots of the breakdown strengths of the nanocomposites are shown in Figure 9, and the characteristic breakdown strengths were used for comparison. These were calculated by treating the breakdown data via a two-parameter Weibull cumulative probability function:  $P(E) = 1 - \exp[-(E/E_0)^\beta]$ .<sup>58</sup> Nine specimens were tested for one sample to fit the function of breakdown strength versus breakdown probability. In the

function,  $E_0$  is the characteristic breakdown strength with a 63.2% cumulative failure probability, and  $\beta$  is a parameter related to linear-regression fit of the data distribution. It can be seen from Figure 9 that although both the BST/P(VDF–HFP) and PPFPA@BST/P(VDF–HFP) nanocomposites exhibit lower breakdown strengths in comparison with P(VDF–HFP), PPFPA@BST/P(VDF–HFP) displays higher breakdown strength than BST/P(VDF–HFP). For example, the characteristic breakdown strengths of BST/P(VDF–HFP) and PPFPA@BST/P(VDF–HFP) with 10% BST NWs are 170.2 and 190.9 MV/m, respectively. In addition, the increase in breakdown strength in PPFPA@BST/P(VDF–HFP) becomes more apparent with increasing BST loading. The enhancement of the breakdown strength in PPFPA@BST/P(VDF–HFP) should be first attributed to the improved interfacial adhesion between PPFPA@BST and P(VDF–HFP) and the improved dispersion of PPFPA@BST in P(VDF–HFP). The former reduces the defects (e.g., voids and pores) resulting from the incompatibility between BST and P(VDF–HFP), while the latter reduces the size of NW agglomerations, resulting in smaller distortions of the local electric field. On the other hand, the low dielectric constant of the PPFPA shell of the PPFPA@BST may be another reason for the enhanced breakdown strength of the PPFPA@BST/P(VDF–HFP) nanocomposites. In our previous research,<sup>39</sup> we demonstrated the role of the electrical properties of the interfacial region in determining the breakdown strength of polymer nanocomposites filled with core–shell-structured polymer@BaTiO<sub>3</sub> nanoparticles. It was concluded that the nanocomposites tend to exhibit enhanced breakdown strength when the dielectric constant of the interfacial region (i.e., the polymer shell of polymer@BaTiO<sub>3</sub>) is lower than that of the polymer matrix. The conclusion is excellently consistent with the result shown in this research.

**Energy Storage of P(VDF–HFP) Nanocomposites.** The electric displacement–electric field ( $D$ – $E$ ) loops for P(VDF–HFP) and the nanocomposites were measured with increasing peak electric field, and the results are shown in Figure 10. From the figure, it can be seen that the maximum polarization of the nanocomposites increases with the gradual addition of BST NWs. At a given loading of BST NWs, the BST/P(VDF–HFP) nanocomposites exhibit slightly higher maximum polarization under the same electric field in comparison with the PPFPA@BST/P(VDF–HFP) nanocomposites. This is mainly attributed to the slightly higher dielectric constant of the BST/P(VDF–HFP) nanocomposites, as shown in Figure 7. It should be

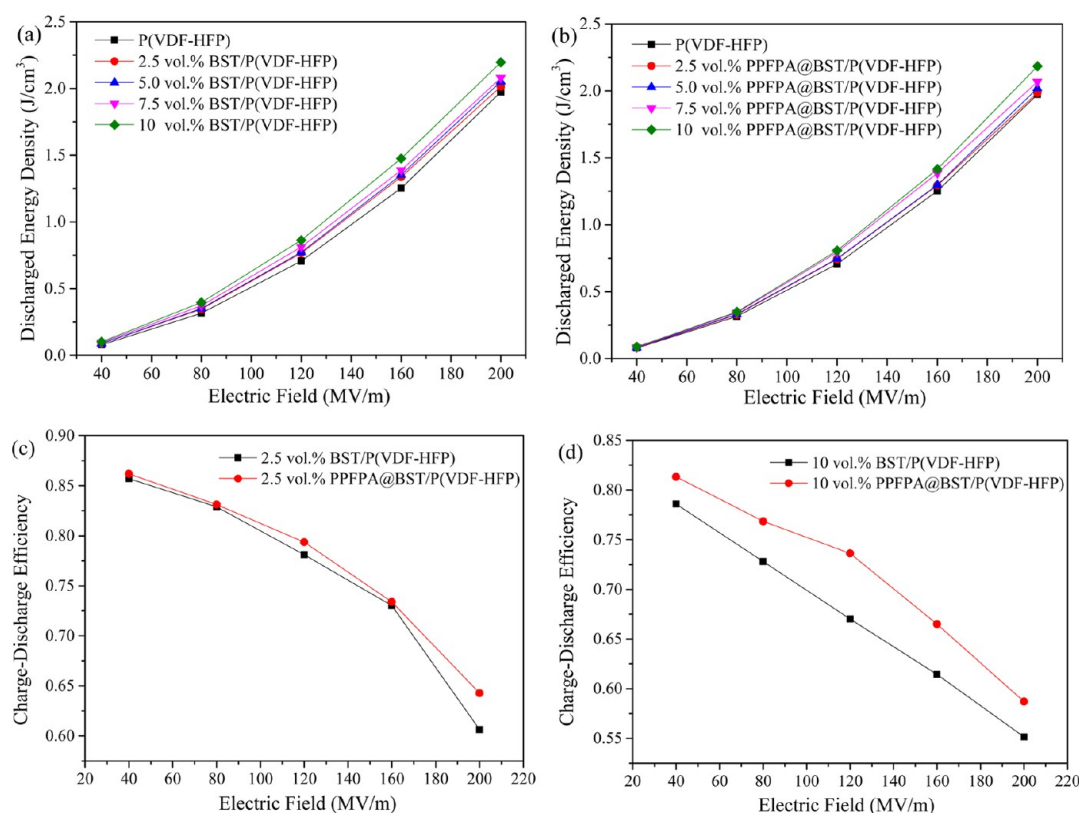


**Figure 11.** (a, b) Discharged energy densities of the P(VDF-HFP)-based nanocomposites. (c, d) Comparison of charge–discharge efficiencies of BST/P(VDF-HFP) and PPFPA@BST/P(VDF-HFP) nanocomposites with (c) 2.5 vol % and (d) 10 vol % BST.

noted that the maximum applied electric field shown in Figure 10 is higher than the breakdown strength of the nanocomposites shown in Figure 9. This is the case mainly because the samples for the breakdown measurement had a large thickness in comparison with those for the measurement of  $D$ – $E$  loops.

Apart from enhancing the breakdown strength of the nanocomposites, the polymer coating of BST NWs was also designed to improve the energy storage efficiency of the nanocomposites. To verify the speculation, the energy densities (both total stored and discharged) and energy efficiencies were calculated according to the  $D$ – $E$  loops shown in Figure 10 using the following equations:

$$U = \int E \, dD \quad (2)$$

$$\text{Eff}_U = \frac{U_{\text{discharged}}}{U_{\text{stored}}} \quad (3)$$

where  $U_{\text{discharged}}$  and  $U_{\text{stored}}$  are the discharged and total stored energy densities, respectively, and  $\text{Eff}_U$  is the energy storage efficiency.<sup>39</sup> The calculated discharged energy densities and energy efficiencies are shown in Figure 11. Both the BST/P(VDF-HFP) and PPFPA@BST/P(VDF-HFP) nanocomposites exhibit increased discharged energy density in comparison with P(VDF-HFP), and the discharged energy densities of the nanocomposites show exponential growth with increasing electric field. Interestingly, although the BST/P(VDF-HFP) nanocomposites have slightly higher dielectric constants (Figure 7) and electric displacements, the two nanocomposites have comparable discharged energy densities. For example, both BST/P(VDF-HFP) and PPFPA@BST/P(VDF-HFP)

with 10% BST have a discharged energy density of about 2.2 J/cm³ at 200 kV/mm, which is 10% higher than that of the pure P(VDF-HFP) films. Such a result indicates that the PPFPA@BST/P(VDF-HFP) nanocomposites should have higher energy storage efficiency. As shown in Figure 11, higher energy storage efficiencies actually were observed for the PPFPA@BST/P(VDF-HFP) nanocomposites. In addition, the increase in the energy storage efficiency becomes more apparent at higher loadings of BST NWs and higher electric fields. These results indicate that, as designed, coating of PPFPA on the surface of the BST NWs is an effective way to increase the energy efficiency. It is a pity that in the current work  $D$ – $E$  loops at electric fields higher than 200 MV/m could not be measured because of the limitation of the high-voltage source. However, much higher enhancement of the maximum discharged energy density and energy storage efficiency can be expected in the PPFPA@BST/P(VDF-HFP) nanocomposites since the nanocomposites have higher breakdown strengths in comparison with the BST/P(VDF-HFP) nanocomposites.

## CONCLUSIONS

P(VDF-HFP) nanocomposites with high power energy density were prepared using core-shell-structured PPFPA@BST NWs as the filler. The PPFPA shell used to encapsulate the BST NWs has a chemical structure and surface energy similar to those of the P(VDF-HFP) matrix, resulting in excellent interfacial adhesion between the NWs and the P(VDF-HFP) matrix. Compared with the as-prepared BST nanocomposites, the PPFPA@BST/P(VDF-HFP) nanocomposites exhibit slightly lower dielectric constant, suppressed leakage current, suppressed dielectric loss tangent at low

frequencies, and enhanced breakdown strength. Although showing slightly lower dielectric constants, the PPFPA@BST/P(VDF-HFP) nanocomposites exhibit discharged energy densities comparable to those of the BST/P(VDF-HFP) nanocomposites because of their low dielectric loss. Importantly, the PPFPA@BST/P(VDF-HFP) nanocomposites exhibit high energy storage efficiencies. In addition, much higher enhancement of the maximum discharged energy density and energy storage efficiency can be expected in the PPFPA@BST/P(VDF-HFP) nanocomposites because of their higher breakdown strength and low dielectric loss.

## AUTHOR INFORMATION

### Corresponding Author

\*E-mail: xyhuang@sjtu.edu.cn.

### Notes

The authors declare no competing financial interest.

## ACKNOWLEDGMENTS

This work was supported by the National Natural Science Foundation of China (51522703, 51277117, and 51477096), the Special Fund of the National Priority Basic Research of China (Grant 2014CB239503), and the State Key Laboratory of Power Systems (Tsinghua University) (Grant SKLD15KZ03). X.H. is thankful for the 2013 SMC Excellent Young Faculty Award of Shanghai Jiao Tong University and Shanghai Pujiang Program (Grant PJ14D018).

## REFERENCES

- (1) Li, Q.; Chen, L.; Gadinski, M. R.; Zhang, S. H.; Zhang, G. Z.; Li, H. Y.; Haque, A.; Chen, L. Q.; Jackson, T.; Wang, Q. Flexible High-Temperature Dielectric Materials from Polymer Nanocomposites. *Nature* **2015**, *523*, 576–579.
- (2) Barber, P.; Balasubramanian, S.; Anguchamy, Y.; Gong, S.; Wibowo, A.; Gao, H. S.; Ploehn, H. J.; Zur Loye, H. C. Polymer Composite and Nanocomposite Dielectric Materials for Pulse Power Energy Storage. *Materials* **2009**, *2*, 1697–1733.
- (3) Li, Q.; Han, K.; Gadinski, M. R.; Zhang, G. Z.; Wang, Q. High Energy and Power Density Capacitors from Solution-Processed Ternary Ferroelectric Polymer Nanocomposites. *Adv. Mater.* **2014**, *26*, 6244–6249.
- (4) Ortiz, R. o. P.; Facchetti, A.; Marks, T. J. High-K Organic, Inorganic, and Hybrid Dielectrics for Low-Voltage Organic Field-Effect Transistors. *Chem. Rev.* **2010**, *110*, 205–239.
- (5) Zhang, Q. M.; Li, H. F.; Poh, M.; Xia, F.; Cheng, Z. Y.; Xu, H. S.; Huang, C. An All-Organic Composite Actuator Material with a High Dielectric Constant. *Nature* **2002**, *419*, 284–287.
- (6) Hardy, C. G.; Islam, M. S.; Gonzalez-DeLozier, D.; Morgan, J. E.; Cash, B.; Benicewicz, B. C.; Ploehn, H. J.; Tang, C. B. Converting an Electrical Insulator into a Dielectric Capacitor: End-Capping Polystyrene with Oligoaniline. *Chem. Mater.* **2013**, *25*, 799–807.
- (7) Dang, Z. M.; Yuan, J. K.; Yao, S. H.; Liao, R. J. Flexible Nanodielectric Materials with High Permittivity for Power Energy Storage. *Adv. Mater.* **2013**, *25*, 6334–6365.
- (8) Tanaka, T.; Montanari, G. C.; Mulhaupt, R. Polymer Nanocomposites as Dielectrics and Electrical Insulation-Perspectives for Processing Technologies, Material Characterization and Future Applications. *IEEE Trans. Dielectr. Electr. Insul.* **2004**, *11*, 763–784.
- (9) Li, J. Y.; Zhang, L.; Ducharme, S. Electric Energy Density of Dielectric Nanocomposites. *Appl. Phys. Lett.* **2007**, *90*, 132901.
- (10) Dang, Z. M.; Yuan, J. K.; Zha, J. W.; Zhou, T.; Li, S. T.; Hu, G. H. Fundamentals, Processes and Applications of High-Permittivity Polymer-Matrix Composites. *Prog. Mater. Sci.* **2012**, *57*, 660–723.
- (11) Claude, J.; Lu, Y. Y.; Li, K.; Wang, Q. Electrical Storage in Poly (Vinylidene Fluoride) Based Ferroelectric Polymers: Correlating Polymer Structure to Electrical Breakdown Strength. *Chem. Mater.* **2008**, *20*, 2078–2080.
- (12) Huang, X. Y.; Jiang, P. K. Core-Shell Structured High-K Polymer Nanocomposites for Energy Storage and Dielectric Applications. *Adv. Mater.* **2015**, *27*, 546–554.
- (13) Hu, P. H.; Shen, Y.; Guan, Y. H.; Zhang, X. H.; Lin, Y. H.; Zhang, Q. M.; Nan, C. W. Topological-Structure Modulated Polymer Nanocomposites Exhibiting Highly Enhanced Dielectric Strength and Energy Density. *Adv. Funct. Mater.* **2014**, *24*, 3172–3178.
- (14) Kim, Y.; Smith, O. N. L.; Kathaperumal, M.; Johnstone, L. R.; Pan, M. J.; Perry, J. W. Enhancement of Breakdown Strength and Energy Density in BaTiO<sub>3</sub>/Ferroelectric Polymer Nanocomposites Via Processing-Induced Matrix Crystallinity and Uniformity. *RSC Adv.* **2014**, *4*, 19668–19673.
- (15) Gao, L.; He, J.; Hu, J.; Li, Y. Large Enhancement in Polarization Response and Energy Storage Properties of Poly(Vinylidene Fluoride) by Improving the Interface Effect in Nanocomposites. *J. Phys. Chem. C* **2014**, *118*, 831–838.
- (16) Yu, D.; Xu, N. X.; Hu, L.; Zhang, Q. L.; Yang, H. Nanocomposites with BaTiO<sub>3</sub>-SrTiO<sub>3</sub> Hybrid Fillers Exhibiting Enhanced Dielectric Behaviours and Energy-Storage Densities. *J. Mater. Chem. C* **2015**, *3*, 4016–4022.
- (17) Zhang, X.; Shen, Y.; Zhang, Q. H.; Gu, L.; Hu, Y. H.; Du, J. W.; Lin, Y. H.; Nan, C. W. Ultrahigh Energy Density of Polymer Nanocomposites Containing BaTiO<sub>3</sub>@TiO<sub>2</sub> Nanofibers by Atomic-Scale Interface Engineering. *Adv. Mater.* **2015**, *27*, 819–824.
- (18) Luo, S. B.; Yu, S. H.; Sun, R.; Wong, C. P. Nano Ag-Deposited BaTiO<sub>3</sub> Hybrid Particles as Fillers for Polymeric Dielectric Composites: Toward High Dielectric Constant and Suppressed Loss. *ACS Appl. Mater. Interfaces* **2014**, *6*, 176–182.
- (19) Tang, H. X.; Lin, Y. R.; Sodano, H. A. Enhanced Energy Storage in Nanocomposite Capacitors through Aligned Pzt Nanowires by Uniaxial Strain Assembly. *Adv. Energy Mater.* **2012**, *2*, 469–476.
- (20) Tang, H. X.; Sodano, H. A. High Energy Density Nanocomposite Capacitors Using Non-Ferroelectric Nanowires. *Appl. Phys. Lett.* **2013**, *102*, 063901.
- (21) Tang, H. X.; Sodano, H. A. Ultra High Energy Density Nanocomposite Capacitors with Fast Discharge Using Ba<sub>0.2</sub>Sr<sub>0.8</sub>TiO<sub>3</sub> Nanowires. *Nano Lett.* **2013**, *13*, 1373–1379.
- (22) Tang, H. X.; Lin, Y. R.; Sodano, H. A. Synthesis of High Aspect Ratio BaTiO<sub>3</sub> Nanowires for High Energy Density Nanocomposite Capacitors. *Adv. Energy Mater.* **2013**, *3*, 451–456.
- (23) Tang, H. X.; Zhou, Z.; Sodano, H. A. Relationship between BaTiO<sub>3</sub> Nanowire Aspect Ratio and the Dielectric Permittivity of Nanocomposites. *ACS Appl. Mater. Interfaces* **2014**, *6*, 5450–5455.
- (24) Liu, S. H.; Zhai, J. W.; Wang, J. W.; Xue, S. X.; Zhang, W. Q. Enhanced Energy Storage Density in Poly (Vinylidene Fluoride) Nanocomposites by a Small Loading of Surface-Hydroxylated Ba<sub>0.6</sub>Sr<sub>0.4</sub>TiO<sub>3</sub> Nanofibers. *ACS Appl. Mater. Interfaces* **2014**, *6*, 1533–1540.
- (25) Liu, S. H.; Zhai, J. W. Improving the Dielectric Constant and Energy Density of Poly (Vinylidene Fluoride) Composites Induced by Surface-Modified SrTiO<sub>3</sub> Nanofibers by Polyvinylpyrrolidone. *J. Mater. Chem. A* **2015**, *3*, 1511–1517.
- (26) Wang, Z. P.; Nelson, J. K.; Hillborg, H.; Zhao, S.; Schadler, L. S. Dielectric Constant and Breakdown Strength of Polymer Composites with High Aspect Ratio Fillers Studied by Finite Element Models. *Compos. Sci. Technol.* **2013**, *76*, 29–36.
- (27) Zhou, Z.; Tang, H. X.; Lin, Y. R.; Sodano, H. A. Hydrothermal Growth of Textured Ba<sub>x</sub>Sr<sub>1-x</sub>TiO<sub>3</sub> Films Composed of Nanowires. *Nanoscale* **2013**, *5*, 10901–10907.
- (28) Kolar, D.; Trontelj, M.; Stadler, Z. Influence of Interdiffusion on Solid Solution Formation and Sintering in the System BaTiO<sub>3</sub>-SrTiO<sub>3</sub>. *J. Am. Ceram. Soc.* **1982**, *65*, 470–474.
- (29) Song, Y.; Shen, Y.; Hu, P. H.; Lin, Y. H.; Li, M.; Nan, C. W. Significant Enhancement in Energy Density of Polymer Composites Induced by Dopamine-Modified Ba<sub>0.6</sub>Sr<sub>0.4</sub>TiO<sub>3</sub> Nanofibers. *Appl. Phys. Lett.* **2012**, *101*, 152904.



- (30) Vaia, R. A.; Maguire, J. F. Polymer Nanocomposites with Prescribed Morphology: Going Beyond Nanoparticle-Filled Polymers. *Chem. Mater.* **2007**, *19*, 2736–2751.
- (31) Roy, M.; Nelson, J. K.; MacCrone, R. K.; Schadler, L. S.; Reed, C. W.; Keefe, R. Polymer Nanocomposite Dielectrics—the Role of the Interface. *IEEE Trans. Dielectr. Electr. Insul.* **2005**, *12*, 629–643.
- (32) Kumar, S. K.; Jouault, N.; Benicewicz, B.; Neely, T. Nanocomposites with Polymer Grafted Nanoparticles. *Macromolecules* **2013**, *46*, 3199–3214.
- (33) Zhu, L.; Wang, Q. Novel Ferroelectric Polymers for High Energy Density and Low Loss Dielectrics. *Macromolecules* **2012**, *45*, 2937–2954.
- (34) Li, J. J.; Claude, J.; Norena-Franco, L. E.; Seok, S. I.; Wang, Q. Electrical Energy Storage in Ferroelectric Polymer Nanocomposites Containing Surface-Functionalized BaTiO<sub>3</sub> Nanoparticles. *Chem. Mater.* **2008**, *20*, 6304–6306.
- (35) Li, J. J.; Khanchaitit, P.; Han, K.; Wang, Q. New Route toward High-Energy-Density Nanocomposites Based on Chain-End Functionalized Ferroelectric Polymers. *Chem. Mater.* **2010**, *22*, 5350–5357.
- (36) Li, Q.; Zhang, G. Z.; Liu, F. H.; Han, K.; Gadinski, M. R.; Xiong, C. X.; Wang, Q. Solution-Processed Ferroelectric Terpolymer Nanocomposites with High Breakdown Strength and Energy Density Utilizing Boron Nitride Nanosheets. *Energy Environ. Sci.* **2015**, *8*, 922–931.
- (37) Yang, K.; Huang, X. Y.; Huang, Y. H.; Xie, L. Y.; Jiang, P. K. Fluoro-Polymer@ BaTiO<sub>3</sub> Hybrid Nanoparticles Prepared Via Raft Polymerization: Toward Ferroelectric Polymer Nanocomposites with High Dielectric Constant and Low Dielectric Loss for Energy Storage Application. *Chem. Mater.* **2013**, *25*, 2327–2338.
- (38) Yang, K.; Huang, X. Y.; Zhu, M.; Xie, L. Y.; Tanaka, T.; Jiang, P. K. Combining Raft Polymerization and Thiol–Ene Click Reaction for Core–Shell Structured Polymer@ BaTiO<sub>3</sub> Nanodielectrics with High Dielectric Constant, Low Dielectric Loss, and High Energy Storage Capability. *ACS Appl. Mater. Interfaces* **2014**, *6*, 1812–1822.
- (39) Zhu, M.; Huang, X. Y.; Yang, K.; Zhai, X.; Zhang, J.; He, J. L.; Jiang, P. K. Energy Storage in Ferroelectric Polymer Nanocomposites Filled with Core–Shell Structured Polymer@ BaTiO<sub>3</sub> Nanoparticles: Understanding the Role of Polymer Shells in the Interfacial Regions. *ACS Appl. Mater. Interfaces* **2014**, *6*, 19644–19654.
- (40) Xie, L. Y.; Huang, X. Y.; Wu, C.; Jiang, P. K. Core-Shell Structured Poly (Methyl Methacrylate)/BaTiO<sub>3</sub> Nanocomposites Prepared by in Situ Atom Transfer Radical Polymerization: A Route to High Dielectric Constant Materials with the Inherent Low Loss of the Base Polymer. *J. Mater. Chem.* **2011**, *21*, 5897–5906.
- (41) Xie, L. Y.; Huang, X. Y.; Huang, Y. H.; Yang, K.; Jiang, P. K. Core@ Double-Shell Structured BaTiO<sub>3</sub>–Polymer Nanocomposites with High Dielectric Constant and Low Dielectric Loss for Energy Storage Application. *J. Phys. Chem. C* **2013**, *117*, 22525–22537.
- (42) Qiao, Y. L.; Islam, M. S.; Wang, L.; Yan, Y.; Zhang, J. Y.; Benicewicz, B. C.; Ploehn, H. J.; Tang, C. B. Thiophene Polymer-Grafted Barium Titanate Nanoparticles toward Nanodielectric Composites. *Chem. Mater.* **2014**, *26*, 5319–5326.
- (43) Kim, P.; Doss, N. M.; Tillotson, J. P.; Hotchkiss, P. J.; Pan, M.-J.; Marder, S. R.; Li, J. Y.; Calame, J. P.; Perry, J. W. High Energy Density Nanocomposites Based on Surface-Modified BaTiO<sub>3</sub> and a Ferroelectric Polymer. *ACS Nano* **2009**, *3*, 2581–2592.
- (44) Kim, P.; Jones, S. C.; Hotchkiss, P. J.; Haddock, J. N.; Kippelen, B.; Marder, S. R.; Perry, J. W. Phosphonic Acid-Modified Barium Titanate Polymer Nanocomposites with High Permittivity and Dielectric Strength. *Adv. Mater.* **2007**, *19*, 1001–1005.
- (45) Paniagua, S. A.; Kim, Y. S.; Henry, K.; Kumar, R.; Perry, J. W.; Marder, S. R. Surface-Initiated Polymerization from Barium Titanate Nanoparticles for Hybrid Dielectric Capacitors. *ACS Appl. Mater. Interfaces* **2014**, *6*, 3477–3482.
- (46) Li, Y.; Tao, P.; Viswanath, A.; Benicewicz, B. C.; Schadler, L. S. Bimodal Surface Ligand Engineering: The Key to Tunable Nanocomposites. *Langmuir* **2013**, *29*, 1211–1220.
- (47) Huang, X. Y.; Xie, L. Y.; Yang, K.; Wu, C.; Jiang, P. K.; Li, S. T.; Wu, S.; Tatsumi, K.; Tanaka, T. Role of Interface in Highly Filled Epoxy/BaTiO<sub>3</sub> Nanocomposites. Part I: Effect of Nanoparticle Surface Chemistry on Processing, Thermal Expansion, Energy Storage and Breakdown Strength of the Nanocomposites. *IEEE Trans. Dielectr. Electr. Insul.* **2014**, *21*, 480–487.
- (48) Song, Y.; Shen, Y.; Liu, H. Y.; Lin, Y. H.; Li, M.; Nan, C. W. Improving the Dielectric Constants and Breakdown Strength of Polymer Composites: Effects of the Shape of the BaTiO<sub>3</sub> Nano-inclusions, Surface Modification and Polymer Matrix. *J. Mater. Chem.* **2012**, *22*, 16491–16498.
- (49) Zhao, B.; Lin, L.; He, D. N. Phase and Morphological Transitions of Titania/Titanate Nanostructures from an Acid to an Alkali Hydrothermal Environment. *J. Mater. Chem. A* **2013**, *1*, 1659–1668.
- (50) Park, K.-I.; Bae, S. B.; Yang, S. H.; Lee, H. I.; Lee, K.; Lee, S. J. Lead-Free BaTiO<sub>3</sub> Nanowires-Based Flexible Nanocomposite Generator. *Nanoscale* **2014**, *6*, 8962–8968.
- (51) Wang, Y.; Zhou, X.; Chen, Q.; Chu, B. J.; Zhang, Q. M. Recent Development of High Energy Density Polymers for Dielectric Capacitors. *IEEE Trans. Dielectr. Electr. Insul.* **2010**, *17*, 1036–1042.
- (52) Yang, K.; Huang, X. Y.; Xie, L. Y.; Wu, C.; Jiang, P. K.; Tanaka, T. Core–Shell Structured Polystyrene/BaTiO<sub>3</sub> Hybrid Nanodielectrics Prepared by in Situ Raft Polymerization: A Route to High Dielectric Constant and Low Loss Materials with Weak Frequency Dependence. *Macromol. Rapid Commun.* **2012**, *33*, 1921–1926.
- (53) Brochu, P.; Pei, Q. B. Advances in Dielectric Elastomers for Actuators and Artificial Muscles. *Macromol. Rapid Commun.* **2010**, *31*, 10–36.
- (54) Teresa Buscaglia, M.; Harnagea, C.; Dapiaggi, M.; Buscaglia, V.; Pignolet, A.; Nanni, P. Ferroelectric BaTiO<sub>3</sub> Nanowires by a Topochemical Solid-State Reaction. *Chem. Mater.* **2009**, *21*, 5058–5065.
- (55) Kang, S. O.; Jang, H. S.; Kim, K. B.; Park, B. H.; Jung, M. J.; Kim, Y. I. Synthesis of Single-Crystal Barium Titanate Nanorods Transformed from Potassium Titanate Nanostructures. *Mater. Res. Bull.* **2008**, *43*, 996–1003.
- (56) Zhou, T.; Zha, J. W.; Cui, R. Y.; Fan, B. H.; Yuan, J. K.; Dang, Z. M. Improving Dielectric Properties of BaTiO<sub>3</sub>/Ferroelectric Polymer Composites by Employing Surface Hydroxylated BaTiO<sub>3</sub> Nanoparticles. *ACS Appl. Mater. Interfaces* **2011**, *3*, 2184–2188.
- (57) Dang, Z. M.; Xu, H. P.; Wang, H. Y. Significantly Enhanced Low-Frequency Dielectric Permittivity in the BaTiO<sub>3</sub>/Poly(Vinylidene Fluoride) Nanocomposite. *Appl. Phys. Lett.* **2007**, *90*, 012901.
- (58) Wang, G. Y.; Huang, X. Y.; Jiang, P. K. Tailoring Dielectric Properties and Energy Density of Ferroelectric Polymer Nanocomposites by High-K Nanowires. *ACS Appl. Mater. Interfaces* **2015**, *7*, 18017–18027.